

NANO EXPRESS

Open Access



CrossMark

Electrical, structural, and optical properties of sulfurized Sn-doped In_2O_3 nanowires

M. Zervos^{1*}, C. N. Mihailescu^{2,5}, J. Giapintzakis², A. Othonos³, A. Travlos⁴ and C. R. Luculescu⁵

Abstract

Sn-doped In_2O_3 nanowires have been grown on Si via the vapor-liquid-solid mechanism at 800 °C and then exposed to H_2S between 300 to 600 °C. We observe the existence of cubic bixbyite In_2O_3 and hexagonal SnS_2 after processing the Sn: In_2O_3 nanowires to H_2S at 300 °C but also cubic bixbyite In_2O_3 , which remains dominant, and the emergence of rhombohedral $\text{In}_2(\text{SO}_4)_3$ at 400 °C. The resultant nanowires maintain their metallic-like conductivity, and exhibit photoluminescence at 3.4 eV corresponding to band edge emission from In_2O_3 . In contrast, Sn: In_2O_3 nanowires grown on glass at 500 °C can be treated under H_2S only below 200 °C which is important for the fabrication of $\text{Cu}_2\text{S}/\text{Sn}:\text{In}_2\text{O}_3$ core-shell p-n junctions on low-cost transparent substrates such as glass suitable for quantum dot-sensitized solar cells.

Keywords: Sulfur; Indium tin oxide; Nanowires

Background

Semiconductor nanowires (NWs) are attractive for the fabrication of nanoscale devices such as nanowire solar cells (NWSCs) and sensors, but some of the main issues pertaining to the realization of high performance devices is doping and control or modification of the surface properties which are important in view of the large surface to volume ratio [1]. For instance the surface modification of III–V NWs such as InAs and GaAs NWs using sulfur has been shown to improve their electrical and optical properties [2–6], but the effect of sulfur on the structural, electrical and optical properties of metal oxide (MO) NWs has not been considered previously, despite the fact that it leads to a suppression of surface recombination and improvement of the photoluminescence (PL) in bulk ZnO [7, 8]. Controlling the surface properties of MO NWs is also necessary in order to suppress the adsorption and desorption of oxygen which is responsible for charge fluctuations and has been achieved so far by using polyimide and polymethyl methacrylate on ZnO and SnO_2 NWs, respectively [9, 10].

Recently, we carried out a systematic investigation into the growth and properties of Sn-doped In_2O_3 or indium tin oxide (ITO) NWs grown on Si by the vapor-liquid-

solid (VLS) mechanism [11] which may be converted to metal oxysulfide (MOxS) NWs with different properties by post growth processing under H_2S that is useful for NWSCs. It has been shown that bulk $\beta\text{-In}_2\text{S}_{3-3x}\text{O}_{3x}$ has an optical band gap that varies from 2.1 eV in pure $\beta\text{-In}_2\text{S}_3$ to 2.9 eV when it contains 8.5 at.% of oxygen and has been proposed as an alternative to CdS buffer layers in $\text{CuIn}_x\text{Ga}_{1-x}\text{Se}_2$ solar cells [12, 13]. In addition, the post growth processing of Sn-doped In_2O_3 NWs under H_2S at different temperatures is important in understanding their properties and limitations as gas sensors which so far has been considered only up to 250 °C [14–16].

Hence, we carried out a systematic investigation into the structural, electrical, and optical properties of Sn-doped In_2O_3 NWs following post growth processing under H_2S between 300 to 600 °C. We observe the existence of cubic bixbyite In_2O_3 and the formation of hexagonal SnS_2 after processing the Sn-doped In_2O_3 NWs under H_2S at 300 °C but also cubic bixbyite In_2O_3 , which remains dominant, and the emergence of rhombohedral $\text{In}_2(\text{SO}_4)_3$ at 400 °C. The Sn-doped In_2O_3 NWs maintain their metallic-like conductivities after exposure to H_2S while we observed the emergence of PL at 3.4 eV corresponding to band edge emission from In_2O_3 in addition to the emission at 2.5 eV which is related to oxygen vacancies and states lying energetically in the upper half of the energy band gap of the as-grown Sn-doped In_2O_3 NWs. Besides the above, we have also

* Correspondence: zervos@ucy.ac.cy

¹Nanostructured Materials and Devices Laboratory, Department of Mechanical and Manufacturing Engineering, P.O. Box 20537, Nicosia 1678, Cyprus

Full list of author information is available at the end of the article

grown Sn-doped In_2O_3 NWs on soda lime glass (SLG) at 500 °C, but we find that a significant deterioration in their conductivity occurs after exposure to H_2S above 200 °C which might be related to Na ion diffusion as it was not observed in the case of the Sn-doped In_2O_3 NWs grown on Si. We discuss the importance of these findings for the fabrication of quantum dot-sensitized solar cells (QDSSCs) consisting of n-type MO NWs like SnO_2 , $\text{Sn:In}_2\text{O}_3$, and p-type chalcogenide semiconductors such as Cu_2S or CuSnS_3 [17].

Methods

Sn-doped In_2O_3 NWs were grown on Si(001) and fused silica by low-pressure chemical vapor deposition (LPCVD) described in detail elsewhere [11]. Square samples of Si and fused silica $\approx 7 \times 7$ mm were cleaned sequentially in trichloroethylene, methanol, acetone, isopropanol, rinsed with de-ionized water, dried with nitrogen, and coated with ≈ 1 nm of Au. For the growth of Sn-doped In_2O_3 NWs, Sn (Aldrich, 2–14 Mesh, 99.9 %), and In (Aldrich, Mesh 99.9 %) were weighed with an accuracy of ± 1 mg. About 0.2 g of In containing ≈ 1 to 5 % wt Sn was used for the growth of the Sn-doped In_2O_3 NWs. Initially the LPCVD tube was pumped down to 10^{-4} mBar and purged with 600 sccm of Ar for 10 min at 1 mBar. Then the temperature was ramped up to 800 °C at 30 °C/min using the same flow of Ar. Upon reaching 800 °C, a flow of 10 sccm O_2 was added in order to grow the Sn: In_2O_3 NWs over 60 min after which cool down took place over 30 min without O_2 . Note that the Sn-doped In_2O_3 NWs were grown on fused silica for 10 min in order to maintain transparency. The morphology of the Sn-doped In_2O_3 NWs was determined by scanning electron microscopy (SEM) while their crystal structure was determined by grazing incidence x-ray diffraction (GIXD) using a Rigaku Smart Lab diffractometer (9-kW rotating Cu-anode) with Cu- $K_{\alpha 1}$ radiation. The Sn-doped In_2O_3 NWs were subsequently treated under a constant gas flow of 20 sccm Ar:50 sccm H_2S between 300 to 600 °C for 60 min using a ramp rate of 10 °C/min but also at 400 °C for 30 min. All of the Sn-doped In_2O_3 NWs were inspected by SEM after post growth processing under H_2S in order to determine changes in morphology while their crystal structure and phase purity was determined by GIXD. Transmission electron microscopy (TEM) was carried out using a FEI CM20 microscope operating at 200 kV while the constituent elements were identified by energy dispersive x-ray analysis (EDX) using a FEI SEM Inspect S equipped with a Si(Li) detector from EDAX Inc. The steady state absorption-transmission spectra were obtained with a Perkin-Elmer UV-vis spectrophotometer and PL using an excitation of 266 nm while ultrafast absorption-transmission spectroscopy was carried out using a Ti:Al₂O₃ ultrafast amplifier generating 100 fs pulses at

800 nm and repetition rate of 1 kHz. Non-linear crystals were used to generate 266/400 nm for the purpose of exciting the Sn-doped In_2O_3 NWs whereas part of the fundamental pulse was used to generate a super continuum light for probing different energy states. Finally, Sn-doped In_2O_3 NWs were also grown at 500 °C on 10 × 20 mm soda lime glass (SLG) slides which were cleaned as described above followed by the deposition of 1 nm Au after which they were treated under H_2S at 100, 200, 300, 400, and 500 °C and their resistance measured with a Kiethley 2635 A in accordance with O'Dwyer et al. [18].

Results and discussion

Sn-doped In_2O_3 NWs were grown by the VLS mechanism on 1 nm Au/Si(001) at 800 °C using 1–5 % Sn [11]. A typical SEM image of the Sn-doped In_2O_3 NWs is shown in Fig. 1a. Their diameters varied between 50 to 100 nm as shown by the inset in Fig. 1a while their lengths reached up to 100 μm . We have shown previously that the Sn-doped In_2O_3 NWs have the cubic bixbyite crystal structure of In_2O_3 as confirmed by GIXD but also by high resolution transmission electron microscopy (HRTEM) analysis which showed that the lattice spacing is equal to 0.718 nm and corresponds to the d-spacing of the {−1,1,0} crystallographic planes of the cubic bixbyite crystal structure of In_2O_3 [11]. However, we also observed the formation of SnO_2 nanoparticles with a tetragonal rutile crystal structure on the surface of the Sn-doped In_2O_3 NWs as shown by the inset of Fig. 1a which is attributed to the limited miscibility and different ionic radii of Sn and In. We do not observe the fluorite structure of $\text{In}_x\text{Sn}_y\text{O}_{3.5}$ as shown recently by Meng et al. [19] who observed a flux-induced crystal phase transition in the VLS growth of Sn-doped In_2O_3 NWs. The PL of the Sn-doped In_2O_3 NWs was found to be broad with a maximum at $\lambda = 500$ nm or 2.5 eV that shifts to 450 nm or ≈ 2.8 eV upon reducing the content of Sn to 1 % which also results into an increase in the carrier lifetime as shown previously by time-resolved PL [11]. The PL of the as-grown Sn-doped In_2O_3 NWs at 2.8 eV, which is shown in Fig. 3, is not related to band edge emission from In_2O_3 , which is an n-type semiconductor with a direct energy band gap of 3.5 eV and a lower indirect gap of 2.6 eV. Instead, the PL at 2.8 eV is attributed to radiative recombination related to oxygen vacancies and states residing energetically in the upper half of the energy band gap of In_2O_3 as we have shown previously from ultrafast absorption-transmission spectroscopy. Furthermore the n-type Sn-doped In_2O_3 NWs had metallic-like conductivities and resistances up to 100 Ω determined from the linear I–V characteristics, shown as an inset in Fig. 3, due to the larger carrier densities of the order of 10^{19} to 10^{20} cm^{-3} [18].

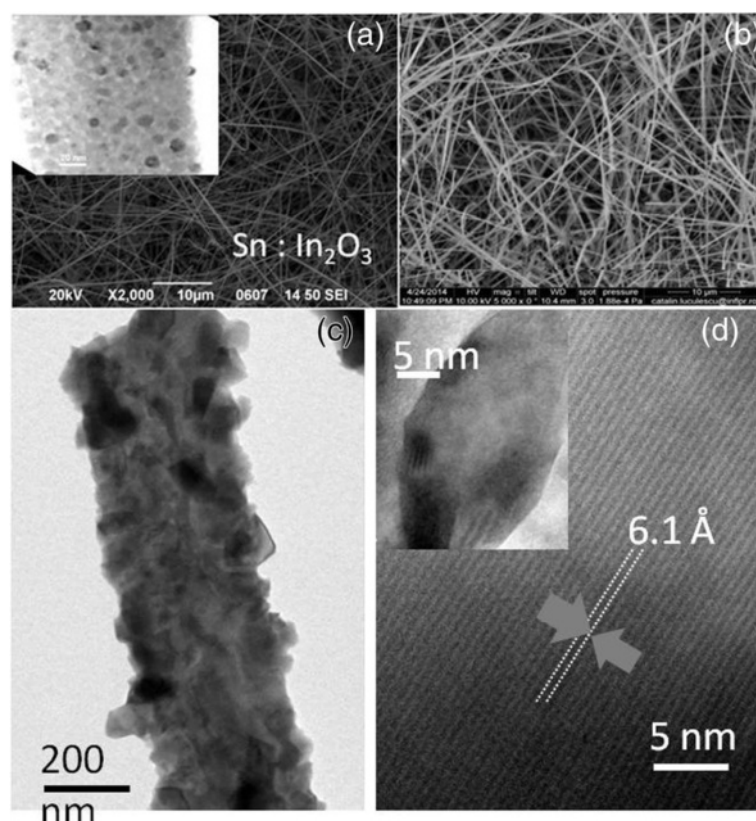


Fig. 1 **a** SEM images of Sn:In₂O₃ NWs on Si(001). inset shows SnO₂ nanoparticles on the surface of the nanowires **(b)** SnS₂:In₂O₃ NWs obtained from Sn:In₂O₃ NWs under H₂S at 300 °C **(c)** high magnification TEM image of the Sn:In₂O₃ NWs processed under H₂S at 400 °C **(d)** HRTEM of the crystals shown in **c** giving a lattice spacing of 6.1 Å corresponding to rhombohedral In₂(SO₄)₃

We consider next the structural, electrical, and optical properties of the Sn-doped In₂O₃ NWs treated under H₂S between 300 to 600 °C. It is well known that H₂S undergoes complete decomposition on the surface of oxides even at room temperature and the S atoms bond to the metal cations of the surface. The ionic radii of O²⁻ and S²⁻ are 1.32 and 1.82 Å, respectively, so we expect that S²⁻ will substitute O²⁻ or fill in vacancies. We find that the Sn-doped In₂O₃ NWs processed under H₂S at 300 °C consist mainly of cubic bixbyite In₂O₃, tetragonal rutile SnO₂, and hexagonal SnS₂ as shown by the GIXD in Fig. 2a where the peaks have been identified according to ICDD 01-071-5323 for SnO₂, ICDD 00-023-0677 for SnS₂, and ICDD 04-012-5550 for In₂O₃. More specifically, we find that the Sn-doped In₂O₃ NWs with 1–2 % Sn are converted into SnS₂/In₂O₃ NWs at 300 °C while we observe SnO₂, SnS₂, and the dominant cubic bixbyite In₂O₃ after exposing the Sn-doped In₂O₃ NWs containing 4 % Sn to H₂S at 300 °C also shown in Fig. 2a. A typical EDX spectrum of the Sn-doped In₂O₃ NWs processed under H₂S at 400 °C confirming the presence of In, Sn, and S is shown as an inset in Fig. 3.

Similarly we observe the cubic bixbyite In₂O₃ but also the emergence of rhombohedral In₂(SO₄)₃, identified using ICDD 00-027-1163, in the GIXD of the Sn-doped In₂O₃ NWs containing 2–4 % Sn after post growth processing under H₂S at 400 °C as shown in Fig. 2b. A high magnification TEM image is shown in Fig. 1c from which one may observe the formation of the In₂(SO₄)₃ crystals on the surface of the Sn-doped In₂O₃ NWs with a lattice spacing of 6.1 Å determined from the HRTEM of Fig. 1d and identified using PDF 83–217. The Sn-doped In₂O₃ NWs did not remain one dimensional above 400 °C probably due to their rapid reduction by the H₂ evolving from the decomposition of H₂S which requires high temperatures in the range 750 to 1250 K. Hence, we consider further the properties of the Sn-doped In₂O₃ NWs processed under H₂S below 500 °C.

The Sn-doped In₂O₃ NWs exposed to H₂S at 300 °C exhibited PL at $\lambda = 340$ nm or 3.4 eV as shown in Fig. 3 corresponding to band edge emission from In₂O₃. The emergence of band edge emission at ≈ 3.4 eV is still accompanied by the broader PL around 500 nm or 2.5 eV observed in the as-grown Sn-doped In₂O₃ NWs. The

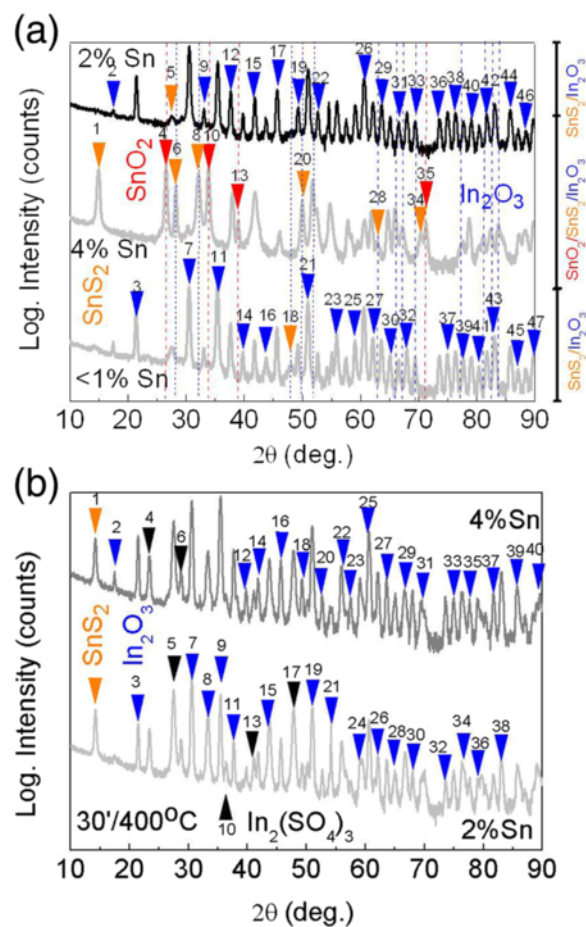


Fig. 2 a GIXD diffraction pattern of Sn:In₂O₃ NWs containing <1 % Sn, 2 % Sn, and 4 % Sn that were exposed to H₂S at 300 °C for 60 min. The peaks have been labeled with increasing angle in ascending order as follows ► 1 (0 0 1), ► 2 (2 0 0), ► 3 (2 1 1), ► 4 (1 1 0), ► 5 (10 0), ► 6 (1 0 0), ► 7 (2 2 2), ► 8 (1 0 1), ► 9 (1 2 3), ► 10 (1 0 1), ► 11 (4 0 0), ► 12 (4 1 1), ► 13 (1 1 1), ► 14 (4 2 0), ► 15 (3 3 2), ► 16 (4 2 2), ► 17 (1 3 4), ► 18 (0 0 3), ► 19 (1 2 5), ► 20 (1 1 0), ► 22 (4 3 3), ► 23 (6 1 1), ► 25 (1 4 5), ► 26 (6 2 2), ► 27 (1 3 6), ► 28 (0 0 4), ► 29 (4 4 4), ► 30 (5 4 3), ► 31 (0 4 6), ► 32 (6 3 3), ► 33 (6 4 2), ► 34 (1 1 3), ► 35 (2 0 2), ► 36 (1 5 6), ► 37 (8 0 0), ► 38 (8 1 1), ► 39 (8 2 0), ► 40 (6 5 3), ► 41 (8 2 2), ► 42 (8 3 1), ► 43 (6 6 2), ► 44 (0 4 8), ► 45 (8 3 3), ► 46 (2 4 8), ► 47 (7 6 1), blue arrows corresponding to In₂O₃, red to SnO₂ and yellow for SnS₂

b GIXD diffraction pattern of Sn:In₂O₃ NWs containing 2 % Sn and 4 % Sn that were exposed to H₂S at 400 °C for 30 min ► 1 (0 0 1), ► 2 (2 0 0), ► 3 (2 1 1), ► 4 (-1 2 1), ► 5 (2 12), ► 6 (0 2 2), ► 7 (2 2 2), ► 8 (1 2 3), ► 9 (4 0 0), ► 10 (2 1 3), ► 11 (4 1 1), ► 12 (4 2 0), ► 13 (0 4 1), ► 14 (3 3 2), ► 15 (4 2 2), ► 16 (1 3 4), ► 17 (1 2 4), ► 18 (1 2 5), ► 19 (4 4 0), ► 20 (4 3 3), ► 21 (6 0 0), ► 22 (6 1 1), ► 23 (0 2 6), ► 24 (1 4 5), ► 25 (6 2 2), ► 26 (13 6), ► 27 (4 4 4), ► 28 (5 4 3), ► 29 (0 4 6), ► 30 (6 3 3), ► 31 (6 4 2), ► 32 (1 5 6), ► 33 (8 0 0), ► 34 (8 1 1), ► 35 (8 2 0), ► 36 (6 5 3), ► 37 (8 3 1), ► 38 (6 6 2), ► 39 (0 4 8), ► 40 (7 6 1) The diffracted peaks are labeled by blue arrows for In₂O₃, yellow for SnS₂ and black for In₂(SO₄)₃ in ascending order and increasing angle

emergence of band edge emission is attributed to a suppression of the surface recombination similar to what has been observed in the case of bulk ZnO [7]. Here, it should be noted that SnS₂ is an indirect band gap

semiconductor but exhibits defect-related PL around 2.0–2.5 eV as we have shown recently by post growth processing of SnO₂ NWs under H₂S [20]. In addition, note that InS has an indirect energy gap of 1.9 eV, β-In₂S₃ is an

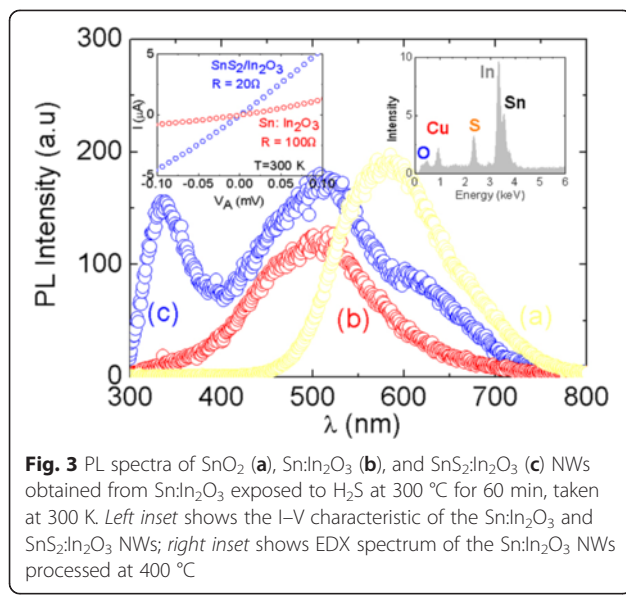


Fig. 3 PL spectra of SnO₂ (**a**), Sn:In₂O₃ (**b**), and SnS₂:In₂O₃ (**c**) NWs obtained from Sn:In₂O₃ exposed to H₂S at 300 °C for 60 min, taken at 300 K. Left inset shows the I-V characteristic of the Sn:In₂O₃ and SnS₂:In₂O₃ NWs; right inset shows EDX spectrum of the Sn:In₂O₃ NWs processed at 400 °C

n-type semiconductor with a direct band gap of 2.1 eV while it has been found that the optical band gap varies from 2.1 eV in pure β -In₂S₃ to 2.9 eV in β -In₂S_{3-x}O_{3x} when it contains 8.5 at.% of oxygen [13]. Consequently the PL the Sn-doped In₂O₃ NWs at \approx 3.4 eV is related to the cubic bixbyite In₂O₃ which is dominant after post growth processing under H₂S between 300 to 400 °C. For completeness, the steady state transmission through the Sn-doped In₂O₃ NWs grown on fused silica at 800 °C before and after post growth processing under H₂S at 200 °C is shown as an inset in Fig. 4. One may observe a slight reduction in the maximum transmission and a small red shift, but the overall shape has not changed, and the maximum occurs at $\lambda \approx 1000$ nm. This red shift is consistent with ultrafast, differential absorption-transmission

spectroscopy measurements, shown in Fig. 4. The differential transmission through the Sn-doped In₂O₃ NWs grown on fused silica between $\lambda = 550$ to 600 nm is positive and decays over a few tens of ps, but we observe a suppression of the $\lambda = 550$ nm trace and increase in differential transmission around $\lambda = 650$ to 700 nm after post growth processing under H₂S as shown by the inset in Fig. 4. This is attributed to the formation of SnS₂ on the surface of the Sn-doped In₂O₃ NWs and is responsible for the red shift observed in the steady state transmission spectrum.

In addition to the optical properties, we find that the Sn-doped In₂O₃ NWs had resistances of \approx 100 Ω, determined from the I-V characteristics shown as an inset in Fig. 3 and maintain their metallic-like conductivity after exposure to H₂S at 300 °C with resistances of \approx 20 Ω.

These findings are important for the realization of p-n junction devices between Sn-doped In₂O₃ NWs in contact with p-type chalcogenide semiconductors like Cu₂S or core-shell Cu₂S/Sn-doped In₂O₃ NWs via the deposition of Cu over Sn-doped In₂O₃ NWs followed by processing under H₂S [17]. Similar core-shell Cu₂S/Sn-doped In₂O₃ NWs have been used as sensors or in QDSSCs by Jiang et al. [21] who decorated n-type Sn-doped In₂O₃ NWs with p-type Cu₂S quantum dots (QDs) using solution-processing methods. In such devices the Sn-doped In₂O₃ NWs that are not covered with Cu₂S QDs come into direct contact with polysulfide liquid electrolytes containing S, Na₂S etc. It is well known that electron-hole recombination at the transparent conducting oxide-liquid electrolyte interface may reduce the overall efficiency. Consequently the deposition of Cu over Sn-doped In₂O₃ NWs followed by its conversion into p-type Cu₂S under H₂S will result into the formation of a core-shell p-n junction but the surface not covered by Cu will be passivated by sulfur which is compatible with polysulfide electrolytes of QDSSCs. Nevertheless one of the challenges in the fabrication of QDSSCs is to grow the Sn-doped In₂O₃ NWs on low-cost transparent substrates such as soda lime glass in order to maintain transparency.

Hence we have grown Sn-doped In₂O₃ NWs on 10 × 20 mm glass slides via the VLS mechanism at temperatures below 600 °C in order to prevent bending and melting. We obtained a high-yield, uniform distribution of Sn-doped In₂O₃ NWs over the 15 × 20 mm glass slide similar to that shown in Fig. 1a. The Sn-doped In₂O₃ NWs had metallic-like conductivities and resistances less than 100 Ω, but the conductivity changed from being metallic to insulator-like after processing under H₂S above 200 °C which we also observed in the case of ITO films on glass. This deterioration in the electrical resistance and conductivity may be related to Na ion diffusion as it was not observed in the case of the Sn-doped In₂O₃

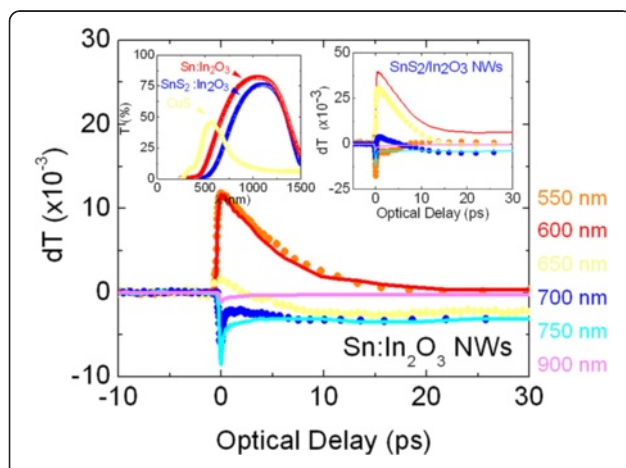


Fig. 4 Ultrafast transient spectroscopy of ITO. Right inset shows the ultrafast transient of the SnS₂:In₂O₃ NWs obtained from the ITO NWs under H₂S at 300 °C for 60 min; left inset shows the steady state absorption-transmission spectra of the ITO and SnS₂:In₂O₃ NWs

NWs grown on Si. Fortunately the Sn-doped In_2O_3 NWs on glass maintain their metallic-like conductivity by processing under H_2S between 100–200 °C which is sufficient for the conversion of Cu into p-type Cu_2S and the realization of p-n junctions.

Conclusions

We have investigated the effect of post growth-processing Sn-doped In_2O_3 NWs under H_2S on their structural, electrical, and optical properties. We observe the existence of hexagonal SnS_2 and cubic bixbyite In_2O_3 which is dominant after exposing the Sn-doped In_2O_3 NWs to H_2S at 300 °C while we also observe the cubic bixbyite In_2O_3 and emergence of orthorhombic $\text{In}_2(\text{SO}_4)_3$ at 400 °C. All of the Sn-doped In_2O_3 NWs maintain their metallic-like conductivity and have resistances between 10 to 100 Ω after processing under H_2S while we also observed the emergence of PL at 3.4 eV corresponding to band edge emission from In_2O_3 . Finally, we have grown Sn-doped In_2O_3 NWs on glass at 500 °C which may be processed under H_2S only between 100 to 200 °C which allows the deposition of Cu over the Sn-doped In_2O_3 NWs and their subsequent conversion into $\text{Cu}_2\text{S}/\text{Sn}:\text{In}_2\text{O}_3$ core-shell p-n junctions for use in QDSSCs.

Competing interests

The authors declare that they have no competing interests.

Authors' contributions

MZ carried out the synthesis of the $\text{Sn}:\text{In}_2\text{O}_3$ NWs and wrote the manuscript; CM and JG did the GIXD; AO carried out the photoluminescence and ultrafast spectroscopy; CL did the EDX, AT did TEM. All authors read and approved the final manuscript.

Author details

¹Nanostructured Materials and Devices Laboratory, Department of Mechanical and Manufacturing Engineering, P.O. Box 20537, Nicosia 1678, Cyprus. ²Nanotechnology Research Center (NRC), P.O. Box 20537, Nicosia 1678, Cyprus. ³Laboratory of Ultrafast Science, Department of Physics, University of Cyprus, P.O. Box 20537, Nicosia 1678, Cyprus. ⁴NCSR Demokritos, Institute of Nanoscience and Nanotechnology, 153 10 Aghia Paraskevi, Athens, Greece. ⁵National Institute for Laser, Plasma and Radiation Physics, Str. Atomistilor, P.O. Box MG-36077125 Magurele, Romania.

Received: 4 March 2015 Accepted: 30 June 2015

Published online: 01 August 2015

References

- Garnett EC, Brongersma ML, Cui Y, Mc Gehee MD. Nanowire Solar Cells. *Ann Rev Mat Res*. 2011;41:269.
- Suyatin D, Thelander C, Bjork M, Maximov I, Samuelson L. Sulfur Passivation for Ohmic Contact Formation to InAs Nanowires. *Nanotechnology*. 2007;18:105307.
- Hughes J, Merchant S, Fu L, Tan H, Jagadish C, Camus EC, et al. Influence of Surface Passivation on Ultrafast Carrier Dynamics and Terahertz Radiation Generation in GaAs. *Appl Phys Lett*. 2006;89:232102.
- Vugt L, Veen S, Bakkers E, Roest A, Vanmaekelbergh D. Increase of the Photoluminescence Intensity of InP Nanowires by Photoassisted Surface Passivation. *J Am Chem Soc*. 2005;127:12357.
- Gutsche C, Niepelt R, Gnauck M, Lysov A, Prost W, Ronning C, et al. Direct Determination of Minority Carrier Diffusion Lengths at Axial GaAs Nanowire p-n Junctions. *Nano Letters*. 2012;12:1453.
- Tajik N, Peng Z, Kuyanov P, La Pierre R. Sulfur Passivation and Contact Methods for GaAs Nanowire Solar Cells. *Nanotechnology*. 2011;22:225402.
- Lahiri J, Senanayake S, Batzill M. Soft x-ray photoemission of clean and sulfur-covered polar ZnO surfaces: A view of the stabilization of polar oxide surfaces. *Phys Rev B*. 2008;78:155414.
- Hwang JY, Park SY, Park JH, Kim JN, et al. Control of ZnO thin film surface by ZnS passivation to enhance photoluminescence. *Thin Solid Films*. 2012;520:1832.
- Huh J, Joo MK, Jang D, Lee JH, Kim GT. Reduced charge fluctuations in individual SnO₂ nanowires by suppressed surface reactions. *J Mater Chem*. 2012;22:24012.
- Park W, Kim J, Yi G, Bae M, Lee H. Fabrication and electrical characteristics of high-performance ZnO nanorod field-effect transistors. *Appl Phys Lett*. 2004;85:5052.
- Zervos M, Mihailescu C, Giapintzakis J, Luculescu CR, Florini N, Kioseoglou J, et al. Broad Compositional Tunability of Indium Tin Oxide Nanowires Grown by the Vapor Liquid Solid Mechanism. *Appl Phys Lett Mats*. 2014;2:056104.
- Barreau N, Marsillac S, Albertini D, Bernede J. Structural, optical and electrical properties of β -In₂S₃-x O₃x thin films obtained by PVD. *Thin Solid Films*. 2002;403:331.
- Zervos M, Papageorgiou P, Othonos A. High yield-low temperature growth of indium sulphide nanowires via chemical vapor deposition. *J Crystal Growth*. 2010;312:656.
- Kaur M, Jainc N, Sharmac K, Bhattacharyya S, Roy M, Tyagi AK, et al. Room-temperature H₂S gas sensing at ppb level by single crystal In₂O₃ whiskers. *Sensors Actuators B*. 2008;133:456.
- Zeng Z, Wang K, Zhang Z, Chen J, Zhou W. The detection of H₂S at room temperature by using indium oxide nanowire transistors. *Nanotechnology*. 2009;20:045503.
- Xu J, Wang X, Shen J. Hydrothermal synthesis of In₂O₃ for detecting H₂S in air. *Sens Actuators B*. 2006;115:642.
- Karageorgou E, Zervos M, Othonos A. Ultraviolet emission from low resistance Cu₂Sn₃/SnO₂ and CulnS₂/Sn:In₂O₃ nanowires. *Appl Phys Mat*. 2014;2:116107.
- O'Dwyer C, Szachowicz M, Visimberga G, Lavayen V, Newcomb SB, Sotomayor Torres CM. Bottom-up growth of fully transparent contact layers of indium tin oxide nanowires for light-emitting devices. *Nat Nanotechnol*. 2009;4:239.
- Meng G, Yanagida T, Yoshida H, Nagashima K, Kanai M, Zhuge F, et al. A flux induced crystal phase transition in the vapor–liquid–solid growth of indium-tin oxide nanowires. *Nanoscale*. 2014;6:7033.
- Zervos M, Mihailescu C, Giapintzakis J, Othonos A and Luculescu CR. 'Surface passivation and the conversion of SnO₂ to SnS₂ nanowires'. *Mat Sci Eng B*. 2015;198:10.
- Jiang Y, Zhang X, Ge QQ, Yu BB, Zou YG, Jiang WJ, et al. ITO@Cu₂S Tunnel Junction Nanowire Arrays as Efficient Counter Electrode for Quantum-Dot-Sensitized Solar Cells. *NanoLetters*. 2014;14:365.

Submit your manuscript to a SpringerOpen® journal and benefit from:

- Convenient online submission
- Rigorous peer review
- Immediate publication on acceptance
- Open access: articles freely available online
- High visibility within the field
- Retaining the copyright to your article

Submit your next manuscript at ► springeropen.com